

Strain-induced tetragonal distortions and multiferroic properties in polycrystalline $\text{Sr}_{1-x}\text{Ba}_x\text{MnO}_3$ ($x = 0.43\text{--}0.45$) perovskites

H. Somaily,¹ S. Kolesnik,¹ J. Mais,¹ D. Brown,¹ K. Chapagain,¹ B. Dabrowski,¹ and O. Chmaissem^{1,2}

¹Physics Department, Northern Illinois University, DeKalb, Illinois 60115, USA

²Materials Science Division, Argonne National Laboratory, Lemont, Illinois 60439, USA



(Received 7 February 2018; published 17 May 2018)

We report the structure-property phase diagram of unique single-ion type-1 multiferroic pseudocubic $\text{Sr}_{1-x}\text{Ba}_x\text{MnO}_3$ perovskites. Employing a specially designed multistep reduction-oxidation synthesis technique, we have synthesized $\text{Sr}_{1-x}\text{Ba}_x\text{MnO}_3$ compositions in their polycrystalline form with a significantly extended Ba solubility limit that is only rivaled by a very limited number of crystals and thin films grown under nonequilibrium conditions. Understanding the multiferroic interplay with structure in $\text{Sr}_{1-x}\text{Ba}_x\text{MnO}_3$ is of great importance as it opens the door wide to the development of newer materials from the parent $(AA')(BB')\text{O}_3$ system with enhanced properties. To this end, using a combination of time-of-flight neutron and synchrotron x-ray scattering techniques, we determined the exact structures and quantified the Mn and oxygen polar distortions above and below the ferroelectric Curie temperature T_C and the Néel temperature T_N . In its ferroelectric state, the system crystallizes in the noncentrosymmetric tetragonal $P4mm$ space group, which gives rise to a large electric dipole moment P_s , in the z direction, of 18.4 and 29.5 $\mu\text{C}/\text{cm}^2$ for $x = 0.43$ and 0.45, respectively. The two independently driven ferroelectric and magnetic order parameters are single-handedly accommodated by the Mn sublattice leading to a novel strain-assisted multiferroic behavior in agreement with many theoretical predictions. Our neutron diffraction results demonstrate the large and tunable suppression of the ferroelectric order at the onset of AFM ordering and confirm the coexistence and strong coupling of the two ferroic orders below T_N . The refined magnetic moments confirm the strong covalent bonding between Mn and the oxygen anions, which is necessary for stabilizing the ferroelectric phase.

DOI: [10.1103/PhysRevMaterials.2.054408](https://doi.org/10.1103/PhysRevMaterials.2.054408)

I. INTRODUCTION

The exciting discovery, two decades ago, of colossal magnetoresistance in manganese-based perovskites led to intense explorations for other exotic ground states in this system including search for thermoelectric and multiferroic properties and materials with enhanced oxygen storage and fuel cell capabilities, etc. The rich playground that the manganites offer arises from a wide range of oxidation states, ionic sizes, and coordination to oxygen that the Mn ions assume, and the delicate balance of a highly flexible structural framework coupled with complex electronic and magnetic properties.

Multiferroics in which two or more order parameters must coexist [1–4] are of great fundamental and technological interest because of their potential for impactful applications with a promise to revolutionize a wide range of consumer electronics in addition to space and defense industries. Although single-ferroic electronic or magnetic materials are relatively abundant, the combination of both orders in one material is relatively scarce and the two orders have long been assumed to be mutually incompatible [2].

Of particular interest to this work is the discovery of multiferroic properties in several oxide materials including BiMnO_3 [5], $\text{Sr}_{1-x}\text{Ba}_x\text{MnO}_3$ (SBMO) [6,7], and BiFeO_3 [3] in addition to a handful of other related rare-earth manganites [1,8,9]. While the sole source of magnetic ordering in these materials is the exchange interaction between localized magnetic moments, the ferroelectric distortion is driven by

a number of distinctly different mechanisms. These include dangling bonds due to A -site lone pairs as in BiMnO_3 [5] and BiFeO_3 [3], charge ordering in $\text{La}_{0.5}\text{Ca}_{0.5}\text{MnO}_3$ [10,11], induced ferroelectric (FE) polarization by magnetic ordering as in the orthorhombic manganite TbMnO_3 [9,12,13], or Y-O mediated dipoles as in the hexagonal manganite YMnO_3 [14], all of which are in clear contrast with the origin of ferroelectricity in the prototypical FE BaTiO_3 , which arises from the combination of empty $3d^0$ shells [15,16] and large strains that force the off-centering displacements of the Ti^{4+} ions.

With the search for new multiferroic materials reaching new heights, theoretical first-principles work predicted that polar distortions [17–19] should exist in alkaline-earth perovskite manganites AMnO_3 ($A = \text{Ca}^{2+}$, Sr^{2+} , or Ba^{2+}) as a consequence of an overly increased A -site ionic size that enhances the local structural strains and promotes ferrodistortive modes via the suppression of the more common antiferrodistortive (AFD) local instabilities [17]. In these studies, it was determined that Ba ions are large enough to stabilize a FE ground state in a hypothetical BaMnO_3 perovskite material and for ferroelectricity to coexist with G-type antiferromagnetic (AFM) ordering [19]. Relatively large strains of $\sim 1\text{--}2\%$ were determined as necessary to induce ferroelectricity in the paraelectric and magnetic SrMnO_3 [18] and CaMnO_3 [17] counterparts. Furthermore, recent *ab initio* calculations [20] showed that if subjected to enough chemical pressures and epitaxial strains, $\text{Sr}_{1-x}\text{Ba}_x\text{MnO}_3$ can be tuned between two distinctly different multiferroic states; one antiferromagnetic state coupled with

small polarization and another ferromagnetic state producing a larger polarization.

The theoretically anticipated multiferroic properties of $\text{Sr}_{1-x}\text{Ba}_x\text{MnO}_3$ were experimentally demonstrated by Sakai *et al.* [7] who correlated the spontaneous polarization of their floating-zone-grown SBMO crystals with strain-induced off-center displacements of the Mn and O ions akin to the singly ferroic BaTiO_3 system. $\text{Sr}_{1-x}\text{Ba}_x\text{MnO}_3$ is classified as a type-I multiferroic system in which independent microscopic origins give rise to the observed ferroelectric and AFM properties [16]. The novelty of SBMO is that the Mn in the Mn–O sublattice is the sole element responsible for both the ferroelectric and magnetic ordering and therefore the coupling between the two order parameters is expected to be strong. Indeed, recent work demonstrated the strong spin-phonon coupling properties [21–23] of SBMO making it, together with its large spontaneous polarization, a promising class of unique multiferroics.

Aside from a few limited investigations, most of the work hitherto on perovskite-type SBMO is either theoretical or performed on thin films and single crystals grown under nonequilibrium conditions. The synthesis of high-quality $\text{Sr}_{1-x}\text{Ba}_x\text{MnO}_3$ (SBMO) polycrystalline samples crystallizing in the pseudocubic perovskite structure is a daunting task as one would have to overcome challenging conditions that usually favor the formation of more stable hexagonal polymorphs as in the well-known hexagonal BaMnO_3 phases, for example [6]. Using an elaborate multistep fabrication technique, we previously produced pure $\text{Sr}_{1-x}\text{Ba}_x\text{MnO}_3$ samples with extended Ba solubility in a narrow phase space range $0 \leq x \leq 0.20$ [6]. The structure of these samples is cubic at all temperatures above their magnetic transitions with no sign observed for ferro- or antiferrodistortive tetragonal distortions (i.e., MnO_6 octahedral rotations and distortions or Mn octahedral off centering). The purpose of this work is to further extend the solubility limit of Ba and to explore the synthesis and structural properties of high-quality bulk materials prepared under highly controlled equilibrium conditions. This includes achieving the desired multiferroicity and the determination by neutron diffraction of accurate values for the Mn^{4+} and O^{2-} atomic displacements in $\text{Sr}_{1-x}\text{Ba}_x\text{MnO}_3$ ($x = 0.43$ and 0.45) that trigger the ferroelectric ordering [7,23]. Results from this work should enable the development of newer multiferroic materials with enhanced properties by single or combined substitutions at the A and/or B sites of the perovskite SrMnO_3 parent structure.

II. SYNTHESIS AND THERMOGRAVIMETRIC MEASUREMENTS

As mentioned above, pseudocubic $\text{Sr}_{1-x}\text{Ba}_x\text{MnO}_3$ perovskites are metastable phases that can only form under stringent synthesis conditions [24]. For this work, high-quality polycrystalline $\text{Sr}_{1-x}\text{Ba}_x\text{MnO}_3$ with $x = 0.43, 0.44,$ and 0.45 materials were prepared from stoichiometric mixtures of SrCO_3 , BaCO_3 , and MnO_2 . In this paper, we report in detail the results of the $x = 0.43$ sample at which ferroelectricity first appears, and the $x = 0.45$ sample, which is the highest Ba concentration achieved in samples with better than 99% purity. In addition, synchrotron x-ray measurements performed on the $x = 0.44$ sample show that it exhibits properties similar to what

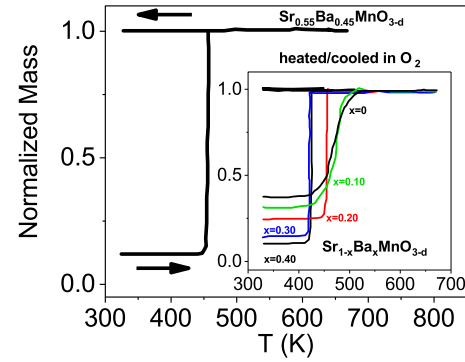


FIG. 1. Thermogravimetric analysis measurements for the as-synthesized $\text{Sr}_{0.55}\text{Ba}_{0.45}\text{MnO}_{3-d}$ sample on heating and cooling (indicated by arrows) in pure oxygen at 1 K/min and held at 670 K for four hours. Inset: Oxygen nonstoichiometry during heating and cooling the perovskite phases $\text{Sr}_{1-x}\text{Ba}_x\text{MnO}_{3-d}$ ($x = 0.0, 0.1, 0.2, 0.3, 0.4$) in pure flowing oxygen under similar conditions.

would be expected for intermediate compositions between the $x = 0.43$ and 0.45 samples.

The perovskite structure was stabilized in a two-step process described elsewhere [6]. In a first step, single-phase oxygen deficient $\text{Sr}_{1-x}\text{Ba}_x\text{MnO}_{3-d}$ perovskite samples were obtained using standard solid-state ceramic fabrication methods with successive grinding and firing at temperatures above 1573 K. In the second step, the oxygen deficient samples are slowly annealed at lower temperatures in a Cahn TG171 thermogravimetric analysis (TGA) furnace in a pure oxygen gas flowing continuously at 100 sccm with heating/cooling rates of 1 K/min until all the oxygen vacancies are completely filled. In order to ensure equilibrium, the samples were soaked at 673 K for four hours. Compacted samples with masses between one and three grams were broken into smaller pieces to help improve the oxygen diffusion during oxygenation. Figure 1 shows the annealing cycle of the reduced $\text{Sr}_{0.55}\text{Ba}_{0.45}\text{MnO}_{3-d}$ sample as a function of temperature normalized to the final sample mass. The oxygen uptake occurs in a single step starting at 450 K. The inset to the figure shows similar curves for other $\text{Sr}_{1-x}\text{Ba}_x\text{MnO}_{3-d}$ compositions treated under similar conditions. The oxygenation temperature at which oxygen vacancies are completely filled and the material becomes fully stoichiometric drops from ~ 460 K for $x = 0$ to ~ 420 K upon increasing the Ba content. It is also worth noting that the oxygenation process concludes much faster with larger concentrations of barium. Additional high oxygen pressure annealing of a few hundred bars followed by very slow cooling to room temperature at a rate of 0.1 K/min were performed to ensure the full oxygen stoichiometry to within ± 0.01 oxygen atom/formula and that no additional oxygen can be incorporated. At a pressure of 225 bar and a temperature of 773 K for example, the careful weighing of the samples before and after annealing did not result in any discernable mass variation thus indicating no change in the oxygen content.

Neutron powder diffraction was performed on the high-resolution time-of-flight (TOF) diffractometer POWGEN at the Spallation Neutron Source of Oak Ridge National Laboratory [25]. Four-gram samples of $\text{Sr}_{0.57}\text{Ba}_{0.43}\text{MnO}_3$ and $\text{Sr}_{0.55}\text{Ba}_{0.45}\text{MnO}_3$ were measured between 10 and 450 K with

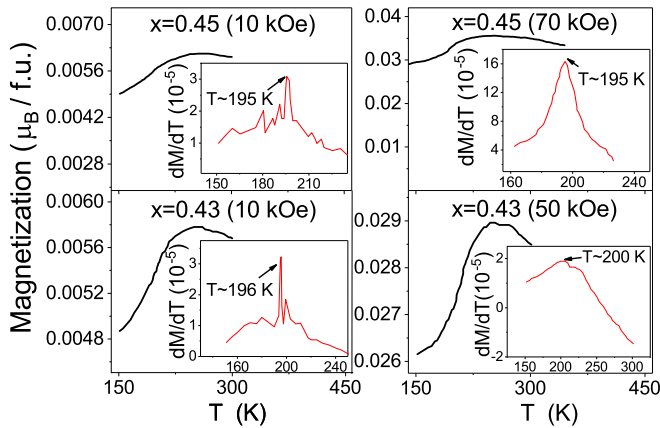


FIG. 2. Direct current magnetization measurements in external magnetic fields between 10 and 70 kOe for $\text{Sr}_{0.57}\text{Ba}_{0.43}\text{MnO}_3$ and $\text{Sr}_{0.55}\text{Ba}_{0.45}\text{MnO}_3$ with clear magnetic transitions observed around 196 ± 5 and 195 ± 5 K, respectively.

the diffraction patterns collected on heating with temperature increments of 20 K. Data were also collected at the high-resolution synchrotron x-ray powder diffraction beam line 11-BM-B at the Advanced Photon Source of Argonne National Laboratory for the $x = 0.43$ – 0.45 compounds at temperatures between 140 and 440 K with increments of 5 K. Rietveld refinements of the structures were performed using the GSAS/EXPGUI software suite [26,27]. Background, peak-profile, and other general variables were refined simultaneously with the lattice parameters, atomic positions, magnetic moment, and isotropic thermal factors. Direct current magnetic measurements were performed using a Quantum Design SQUID in external magnetic fields up to 70 kOe.

III. RESULTS AND DISCUSSION

The dc magnetization (M) measured in a magnetic field range of 10–70 kOe is shown in Fig. 2 for $\text{Sr}_{0.57}\text{Ba}_{0.43}\text{MnO}_3$ and $\text{Sr}_{0.55}\text{Ba}_{0.45}\text{MnO}_3$ together with its first derivative with respect to temperature (dM/dT). A dM/dT peak corresponding to the maximum magnetization slope (kink in the M - T curve) is observed at 196 ± 5 and 195 K for the $x = 0.43$ and 0.45 samples, respectively, in agreement with the neutron diffraction results.

The extended Ba solubility limit shown in Fig. 3 delineates the compositional phase space of the ferroelectric (FE) and multiferroic (MF) materials. The figure shows that the parent cubic $Pm\bar{3}m$ structure fails to distort for all the $x < 0.43$ synthesized compositions despite the significant strains they are subjected to. At low temperatures, these materials with half-filled t_{2g} orbitals, exhibit the expected G-type antiferromagnetic structure [6] with the Néel temperature, T_N , slightly decreasing with increasing Ba (~ 230 – 185 K) in agreement with recent theoretical work [28]. The achievement of ferrodistortive properties is attained with larger A-site ionic size average accomplished by the Ba^{2+n} substitution (ionic size radius $R = 1.61$ Å for twelve-coordinated Ba) for Sr^{2+} (1.44 Å) [29]. In this section, we study the desired ferroelectric distortions in bulk $x \sim 0.43$ – 0.45 samples with transition temperatures, T_C , ranging between 330 and 362 K. More

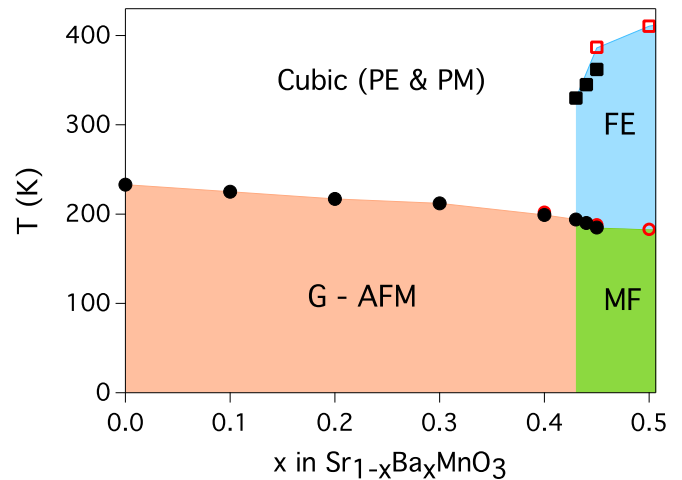


FIG. 3. Phase diagram of the structural, magnetic, and ferroelectric properties as a function of barium content (x) in the multiferroic $\text{Sr}_{1-x}\text{Ba}_x\text{MnO}_3$ system. PE, PM, FE, MF refer to paraelectric, paramagnetic, ferroelectric, and multiferroic properties, respectively. Transitions to a G-type antiferromagnetic phase (G-AFM) are denoted by filled circles for the data taken from our current (this paper) and previous work [6,34] and by the open symbols from Sakai *et al.* [7]. Magnetic and ferroelectric order parameters (MF region) coexist at $x = 0.43$ and above. Please see text for more details.

importantly, we demonstrate the tunable coupling strength of the ferroelectric and magnetic order parameters accomplished by tiny variations of the material’s cationic stoichiometry.

The paraelectric (cubic) to ferroelectric (tetragonal) structural transition line shown in Fig. 3 is relatively broad. While $\text{Sr}_{0.60}\text{Ba}_{0.40}\text{MnO}_3$ does not provide any evidence for long- or short-range tetragonal distortions, these distortions first appear with $x \sim 0.43$ and increase steeply in a very small Ba substitution range. The cla ratio, corresponding to the degree of strain-induced tetragonality, increases to a maximum of 1.0051 and 1.006 at $T = 250$ K for $\text{Sr}_{0.57}\text{Ba}_{0.43}\text{MnO}_3$ and $\text{Sr}_{0.56}\text{Ba}_{0.44}\text{MnO}_3$, respectively. Likewise, the tetragonal transition temperature T_C rises sharply from around room temperature for $\text{Sr}_{0.57}\text{Ba}_{0.43}\text{MnO}_3$ to about 362 K and 420 K for the $x = 0.45$ sample (this work) and $x = 0.5$ [7,23], respectively.

At temperatures above T_C , the $x = 0.43$ – 0.45 samples crystallize in the common cubic $Pm\bar{3}m$ space group symmetry [30,31] with consistent structural refinement reliability factors χ^2 and R_{wp} of about 2.8 and 5%, respectively. The cubic structure is best described as a three-dimensional stack of regular corner-sharing MnO_6 octahedra with the exact center of the octahedral cavities occupied by Sr or Ba [32].

Progressive deterioration of the reliability factors below T_C (with χ^2 becoming as large as 25 at 300 K) is observed if one continues to impose the cubic symmetry as shown in Fig. 4 ($x = 0.43$ and 0.45 for time-of-flight neutron refinements) and Fig. 5 ($x = 0.44$ from synchrotron x-ray APS data). This expected result signals the onset of a phase transition to a lower symmetry in agreement with the clear splitting of various characteristic peaks observed in both the neutron and x-ray diffraction patterns; see Fig. 6 for example. We define the ferroelectric Curie transition temperature T_C as the temperature

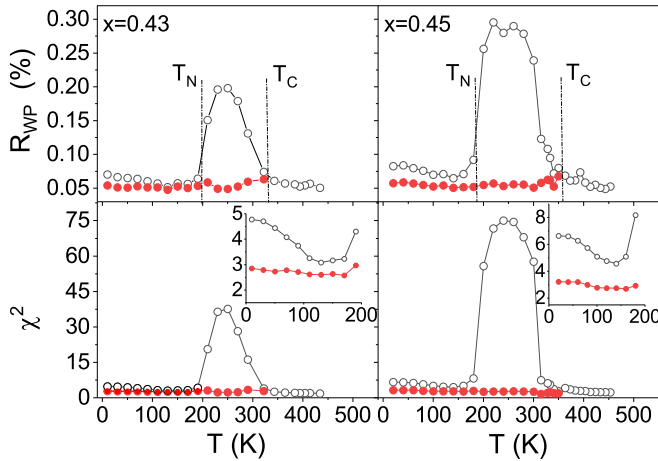


FIG. 4. Left panels ($\text{Sr}_{0.57}\text{Ba}_{0.43}\text{MnO}_3$), right panels ($\text{Sr}_{0.55}\text{Ba}_{0.45}\text{MnO}_3$): Weighted profile residual agreement factor and the goodness of fit χ^2 obtained from time of flight neutron diffraction refinements using cubic $Pm\bar{3}m$ (open circles) and noncentrosymmetric tetragonal $P4mm$ (filled circles) space groups. Significant improvements in the refinements are obtained below T_N when assuming the tetragonal polar symmetry.

of cubic to tetragonal structural transition. Given the relative width of the ferroelectric transition, T_C is determined from the divergence of the Rietveld agreement factors obtained with fits performed using both the cubic and tetragonal models.

While various possible polar structures have been observed and proposed for the ferroelectric BaTiO_3 analog [33], our structural refinements together with previous work [7,23,34] indicate the stability of only one single tetragonal symmetry for SBMO persisting between the ferroelectric and magnetic transition temperatures. Due to favorable displacements of the manganese and oxygen ions from their equilibrium positions,

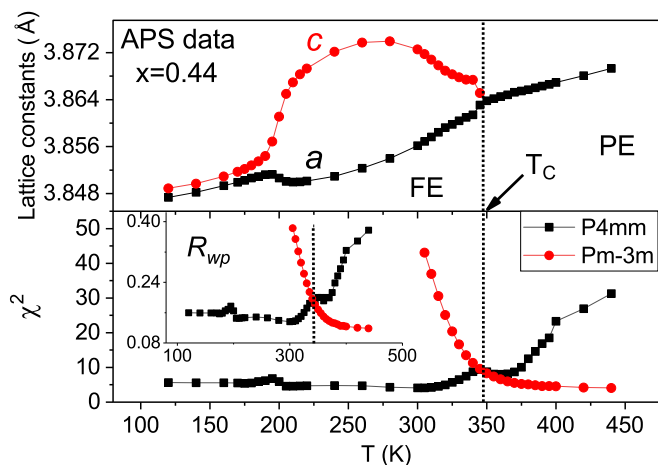


FIG. 5. Top: Refined lattice constants of $\text{Sr}_{0.56}\text{Ba}_{0.44}\text{MnO}_3$ as obtained from APS high-resolution synchrotron x-ray diffraction refinements. Bottom: The ferroelectric Curie transition temperature $T_C = 345$ K of cubic to tetragonal structural transition determined from the divergence of the Rietveld agreement factors. Significant improvements in the refinements are obtained below T_C when assuming the tetragonal polar symmetry.

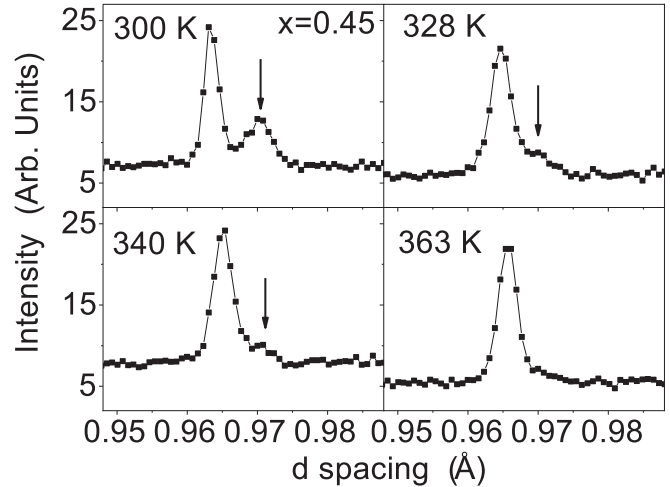


FIG. 6. High-temperature TOF NPD for $\text{Sr}_{0.55}\text{Ba}_{0.45}\text{MnO}_3$ at selected temperatures in the narrow d -spacing range of $0.95\text{--}0.98$ Å showing the sustained splitting of the 400 peak in the ferroelectric region at room temperature and up to $T_C \sim 362$ K above which the structure becomes cubic paraelectric.

the tetragonal distortions of SBMO are best described using the noncentrosymmetric symmetry of the $P4mm$ space group [7]. The displacement of the Mn ions away from their original central positions coupled with the concomitant displacement of the equatorial oxygen atoms in the opposite direction give rise to the tetragonal elongation of the c axis and the associated ferroelectric order. This behavior is similar to the observed Ti and O opposite displacements in tetragonal BaTiO_3 at the temperature range $\sim 280\text{--}400$ K [31].

Time-of-flight neutron data collected at selected temperatures are shown in Fig. 7 for the $\text{Sr}_{0.57}\text{Ba}_{0.43}\text{MnO}_3$ sample. Figure 8 shows synchrotron x-ray powder diffraction data for the $\{200\}$ reflection for the $x = 0.43\text{--}0.45$ samples. In all samples, minute traces of the MnO impurity phase, with a refined weight fraction of no more than $0.5\text{--}0.6\%$, were observed (crosses) and successfully included in the refinements and final fits. Tetragonal splitting of characteristic peaks (e.g.,

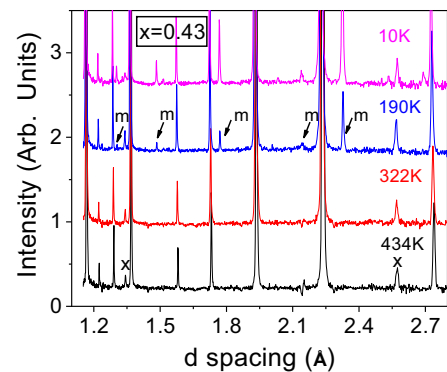


FIG. 7. Time-of-flight neutron-diffraction patterns in a 1.6 Å wide d -spacing range showing reflections for $\text{Sr}_{0.57}\text{Ba}_{0.43}\text{MnO}_3$ at select temperatures. Cross symbols correspond to a small MnO impurity phase ($\sim 0.6\%$ by weight) while the arrows indicate magnetic reflections that arise from antiferromagnetic ordering below T_N .

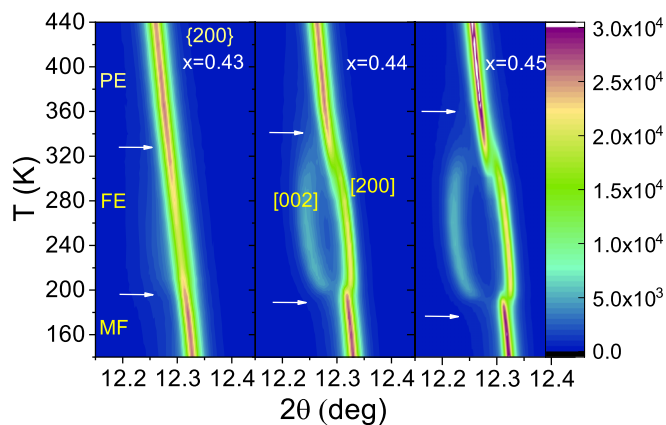


FIG. 8. Contour maps of the cubic $\{200\}$ reflection from synchrotron x-ray powder diffraction for the $x = 0.43, 0.44$ [34], and 0.45 samples. The tetragonal splitting of the peak is observed at T_C (top arrows), which changes as a function of the Ba content. The splitting is partially suppressed below T_N (bottom arrows).

$[002]$ and $[200]$ in Fig. 8) is observed in the diffraction patterns below T_C followed by the partial suppression of the tetragonal order below T_N and the appearance of new magnetic peaks (arrows in Fig. 7).

As the temperature approaches the magnetic transition on cooling, the cla ratio shown in Fig. 9 for $\text{Sr}_{0.57}\text{Ba}_{0.43}\text{MnO}_3$ collapses sharply to indicate the suppression of the tetragonal distortion with a possible return to the high-temperature cubic symmetry. The complete or partial suppression of the tetragonal order can be determined by carefully examining the behavior of characteristic peaks below T_N . Indeed, while the tetragonal $\{400\}$, $\{311\}$, $\{220\}$, and $\{200\}$ peaks are no longer split they remain significantly broader than their corresponding cubic peaks in the paraelectric region above T_C leading us to conclude that the tetragonal distortion is not fully suppressed. Additionally, significantly better agreement factors are obtained with the refinements performed assuming

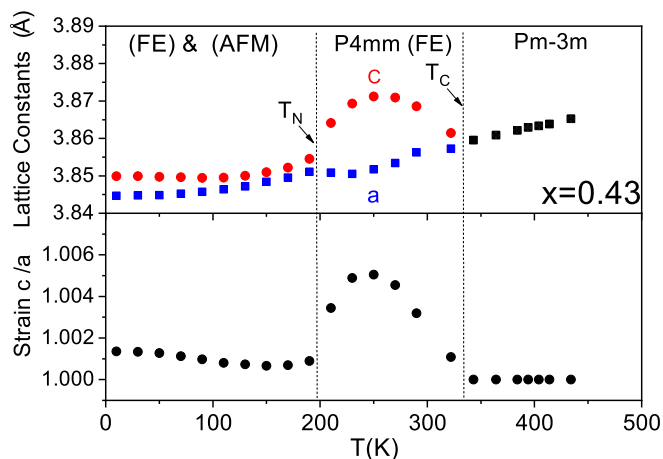


FIG. 9. Top: Refined lattice parameters as a function of temperature for $\text{Sr}_{0.57}\text{Ba}_{0.43}\text{MnO}_3$. Error bars are smaller than the symbol size. Bottom: Tetragonal distortion in this material given as the ratio of lattice constants c/a , which equals unity in the cubic phase. A maximum value of 1.0051 recorded in the FE region at 250 K.

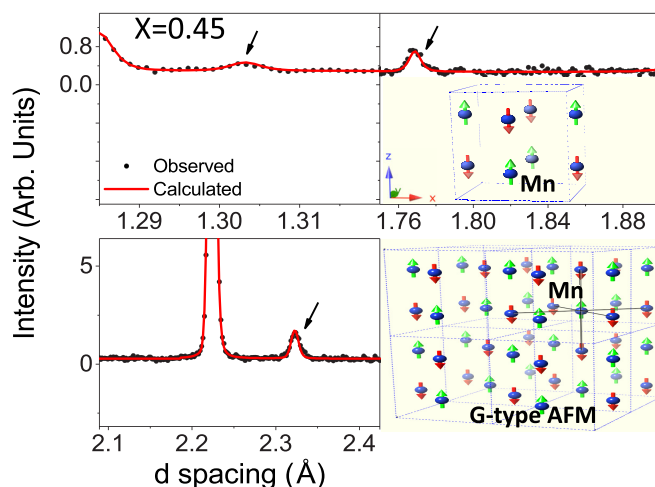


FIG. 10. Selected diffraction peaks (indicated by arrows) for the $x = 0.45$ sample arising from magnetic ordering on the Mn^{4+} sublattice at $T = 40$ K, which were properly fit with the $P4/m'm'm$ magnetic space group symmetry. The inset shows the directions of energetically favored magnetic moments exhibiting a G-type AFM ordering in an extended cell view.

a continuous $P4mm$ symmetry below T_N instead of a return to the cubic symmetry, Fig. 4.

While the nuclear structure is noncentrosymmetric $P4mm$, the antiferromagnetic structure of the Mn sublattice alone (excluding the surrounding oxygen octahedra) is best described using the higher symmetry of the centrosymmetric tetragonal $P4/mmm$ space group. Regardless of whether the material exhibits ferroelectric properties or not, magnetic ordering requires that the cubic structure distorts to become tetragonal below T_N in agreement with discussions made in the preceding paragraph. From a crystallographic perspective, the magnetic symmetry is described as $P4/m'm'm$, which is the result of taking the time-reversal symmetry of the plane mirrors normal to the four- and twofold symmetry axes along the $[001]$ and $[100]/[010]$ directions, respectively. Such spin arrangement results in a G-type AFM ordering where the direction of the magnetic moment of each Mn^{4+} ion is opposite to its six nearest neighbors as shown in Fig. 10. Also shown in the same figure are selected magnetic diffraction peaks for the $x = 0.45$ sample successfully modeled with the magnetic $P4/m'm'm$ symmetry. The refined magnetic moment as a function of temperature is presented in Fig. 11. We find that the temperature dependence of the magnetic moment (μ) can be well fit using a power-law function of the form: $\mu(T) = \mu_0(1 - T/T_N)^\alpha$. The obtained values for T_N are in good agreement with those determined by Rietveld refinements and take the values of 194 and 185 K for the $x = 0.43$ and 0.45 samples, respectively. For both samples, the critical exponent (α) converges to 0.12–0.13, which is comparable to the critical exponent value of two-dimensional (2D) Ising materials ($\alpha = 1/8$).

Figure 12 shows the evolution of the lattice parameters and Néel temperature T_N as a function of the Ba content. The refined lattice parameters as a function of temperature are shown in Figs. 5, 9, and 13 for $x = 0.44, 0.43$, and 0.45 , respectively. In all samples, the high-temperature cubic lattice parameter a exhibits a slight thermal contraction on cooling,

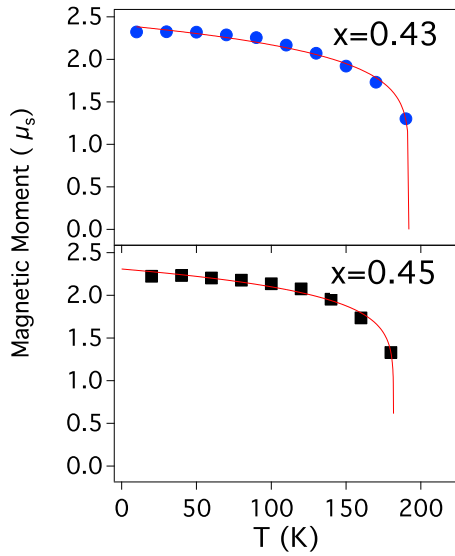


FIG. 11. Refined magnetic moments obtained from time-of-flight neutron diffraction data. A power law was fit to the moments from which the obtained T_N values ($\mu_s = 0$) are in good agreement with values determined from the Rietveld refinements as described in the text and the magnetic measurements.

typical of similar oxides, as it approaches the ferroelectric transition temperature. The lattice distortion expressed as the ratio of lattice parameters c/a serves as an approximate measure for the ratio of the average apical Mn–O1 to equatorial Mn–O2 bond lengths [35] and hence can be directly related to the magnitude of the polarization [7]. There exists a relatively narrow region over which the lattice distortion (c/a ratio)

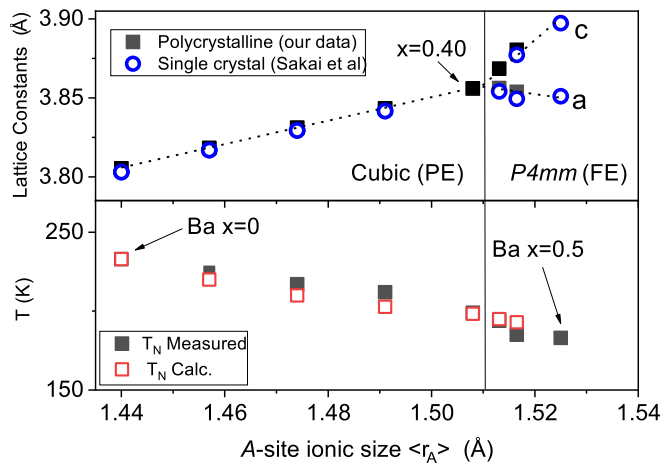


FIG. 12. Top: Room temperature lattice constants of the SBMO materials where the FE tetragonal $P4mm$ distortion is first observed at $x = 0.43$. Tetragonal distortion (c/a) (not shown) increases progressively from this composition on. Dotted line is a guide to the eye. Bottom: Continuously decreasing magnetic transitions T_N from their maximum value of 233 K for Ba-free SrMnO_3 . See text for more details. Measured T_N transitions compared to values calculated using an expression that takes into account the influence of bond angle buckling and A-site ionic size variance as described in this work and in Ref. [6].

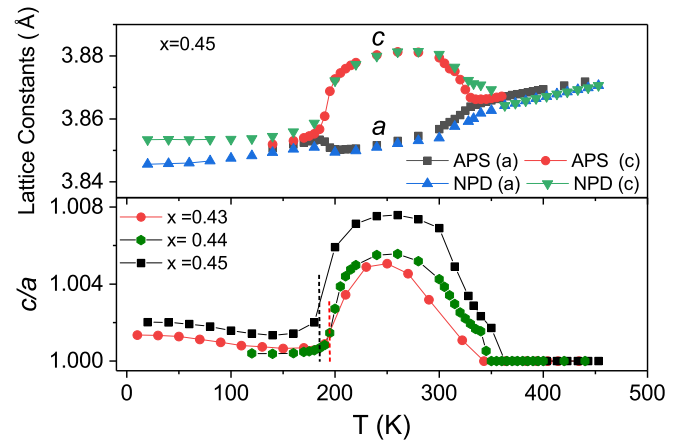


FIG. 13. Top: Temperature evolution of the lattice parameters of $\text{Sr}_{0.55}\text{Ba}_{0.45}\text{MnO}_3$ determined from synchrotron x-ray (11-BM-B) and from TOF neutron diffraction data (POWGEN). Ferroelectric tetragonal distortions are drastically reduced upon approaching magnetic ordering below ~ 195 K demonstrating the strong magnetoelastic coupling in this system. Bottom: Large strain-induced tetragonal distortion shown as c/a for $\text{Sr}_{0.55}\text{Ba}_{0.45}\text{MnO}_3$ compared to the consistently smaller distortion values in $\text{Sr}_{0.57}\text{Ba}_{0.43}\text{MnO}_3$ and $\text{Sr}_{0.56}\text{Ba}_{0.44}\text{MnO}_3$ at all the measured temperatures.

increases rapidly to reach maximum values at $T \sim 260$ K of ~ 1.005 , 1.006 , and 1.008 for $x = 0.43$, $x = 0.44$, and 0.45 , respectively as shown in Fig. 13.

The ferroelectric distortion below T_N is alleviated in various degrees by the magnetic ordering and consequently the c lattice parameter drops to values comparable to a as discussed above. However, when the temperature is further lowered, the tetragonal distortion increases again and the gap between the a and c lattice parameters widens. This structural trend of the ratio c/a bears a strong resemblance to the temperature evolution of the soft mode, which is associated with ferroelectric ordering as observed in spectroscopic studies [21]. It has been found that the soft mode frequency sharply drops at the onset of magnetic transition but continues to harden at the lowest temperatures. Since the soft mode is a direct measure of polarization [36], this indicates a strong coupling between strains and polarization in our materials.

Figure 14 shows the refined atomic positions as a function of temperature for $\text{Sr}_{0.57}\text{Ba}_{0.43}\text{MnO}_3$ and $\text{Sr}_{0.55}\text{Ba}_{0.45}\text{MnO}_3$. As discussed above, our neutron refinement results demonstrate that the Mn and O ions in the ferroelectric regime displace in directions similar to that of the prototypical ferroelectric BaTiO_3 [33] with the Mn atoms shifting along the $-z$ direction while the oxygen atoms (O1 and O2) displace independently along the $+z$ direction. We also demonstrate a strong influence/coupling of the magnetic ordering to ferroelectricity manifested by the partial to near complete suppression of these displacements below T_N .

In a centrosymmetric MnO_6 octahedral cage, the two apical (along the c axis) bond lengths [Mn–O1] are equal in magnitude and the same can be said about the other four planar (in the ab plane) [Mn–O2] bond lengths leading to a zero-sum electric dipole. On the other hand, in the $P4mm$ phase, our neutron refinements show that the octahedra deform into three

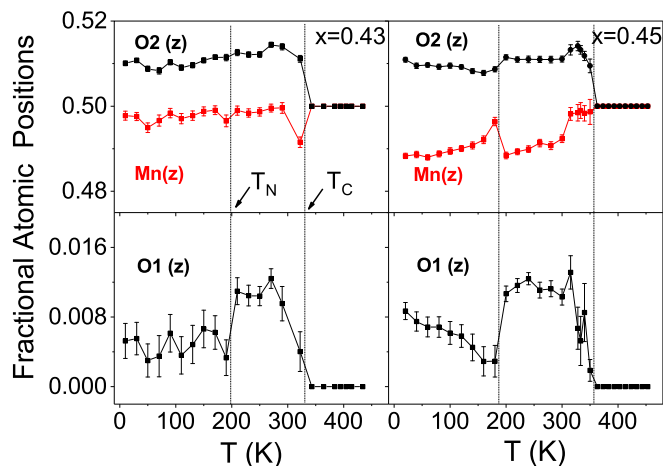


FIG. 14. Fractional z coordinates as a function of temperature for Mn and O refined using neutron powder TOF diffraction data for $\text{Sr}_{0.57}\text{Ba}_{0.43}\text{MnO}_3$ (left panels) and $\text{Sr}_{0.55}\text{Ba}_{0.45}\text{MnO}_3$ (right panels). Displacements of the apical (O1) and planar/equatorial (O2) oxygen atoms as well as the Mn atoms are all along the c -axis direction with z Wyckoff sites given as $(0 + u)$, $(\frac{1}{2} + v)$, and $(\frac{1}{2} - w)$, respectively.

distinct bond lengths whose temperature evolution is shown in Fig. 15. A pronounced distortion is observed for the apical bond length Mn–O1 due to the Mn displacement along the c axis towards one of the two apical oxygen ions to form a strong covalent bond. Consequently, this creates alternating long and short Mn–O1 bonds along the c axis with the short bond being comparable with the equilibrium Mn–O bond length ($\sim 1.897 \text{ \AA}$ [37]). Conversely, the uniformly spaced medium-length Mn–O2 shows a smooth thermal compression across the different phase boundaries. The lowest octahedral distortion is

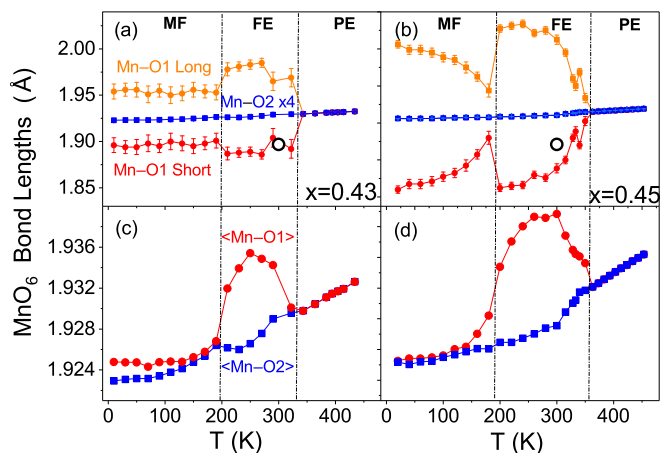


FIG. 15. Top: Detailed temperature evolution of the individual Mn–O bond lengths in MnO_6 octahedra for both the $x = 0.43$ and 0.45 materials. Bottom: The average $\langle \text{Mn–O1} \rangle$ apical bonds exhibit a significant distortion, which is greatly reduced when the magnetic moments order below T_N . Vertical lines correspond to the ferroelectric and magnetic transitions of the materials. At T_C and as the unit cell expands in response to large Ba substitution, the Mn^{4+} ions shift towards one of the apical oxygen atoms in order to retain an equilibrium interatomic Mn–O distance ($\sim 1.897 \text{ \AA}$) [37] shown as open circles.

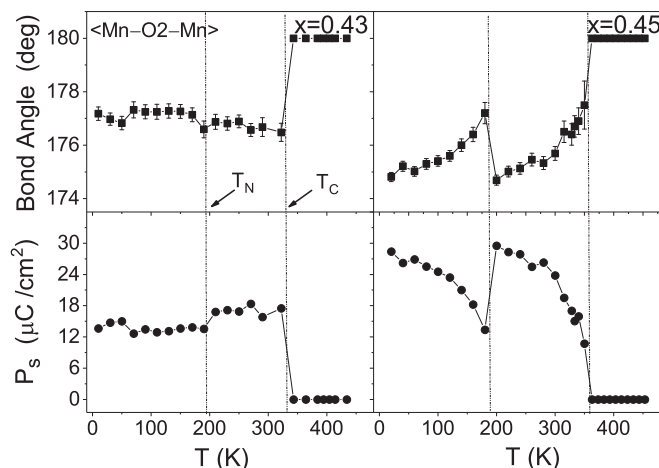


FIG. 16. Top: Measured $\langle \text{Mn–O2–Mn} \rangle$ bond angle as a function of temperature. Below T_N , the bond angle in $\text{Sr}_{0.57}\text{Ba}_{0.43}\text{MnO}_3$ (left panel) is essentially constant with an average value of $\sim 177^\circ$ while in $\text{Sr}_{0.55}\text{Ba}_{0.45}\text{MnO}_3$ it exhibits a wider range of values. Bottom: Spontaneous polarization P_s calculated from the measured bond lengths and bond angles. P_s is very sensitive to the magnitude and variations of the bond angle.

recorded at temperatures near the magnetic ordering transition (T_N) for both samples.

In the paraelectric region (above T_C), the atomic special positions are all fixed by the high symmetry structure resulting in zero polarization. Because of the atomic displacement below T_C , the $\langle \text{O2–Mn–O2} \rangle$ bond angle buckles to values less than the ideal 180° while the apical $\langle \text{O1–Mn–O1} \rangle$ angle remains straight at all temperatures as shown in Fig. 16. The length difference between the two apical bonds [Mn–O1] leads to a net electric dipole in the $-z$ direction. Likewise, the four equidistant equatorial bonds [Mn–O2] produce a net dipole moment canceling out in the ab plane but with a vertical component in the same direction as the apical bonds dipole. Thus, the net electric dipole of the MnO_6 octahedron with a nonzero component in the $-z$ axis can be directly computed from the refined structure, see Fig. 16 (in units of C m) as:

$$|\vec{P}| = q \left\{ \Delta[\text{Mn–O1}] + \left(4 \times [\text{Mn–O2}] \times \sin \frac{180^\circ - \langle \text{Mn–O2–Mn} \rangle}{2} \right) \right\},$$

where $q = 1.95 |e|$, is the electronegativity difference between Mn^{4+} and O^{2-} ions times the electron charge. It then follows from the expression above that the polarization is expected to be quite sensitive to the magnitude of the bond angle, which on the other hand influences the superexchange interactions. The maximum net spontaneous polarization is calculated as $P_s = 18.4 \mu\text{C}/\text{cm}^2$ and $29.5 \mu\text{C}/\text{cm}^2$ for the $x = 0.43$ and 0.45 samples, respectively. It is worth noting the large polarization achieved in this system and how similar it is to that of the BaTiO_3 benchmark ferroelectrics.

Previous arguments have been made for the strong correlation between the magnetic ordering temperatures and the average $\langle \text{Mn–O–Mn} \rangle$ bond angle (θ) [28,37]. While a linear relationship between T_N and $\cos^2\theta$ is well established for

the rare-earth manganites RMnO_3 [37,38], one can see from Fig. 12 that T_N in the SBMO series is clearly a decreasing function of the Ba content even in the cubic regime (with 180° Mn–O–Mn bond angles). As shown in previous work [6], this observed decrease from $T_{N(\text{max})} = 233$ K for the parent SrMnO_3 cannot be explained by solely considering the bond angle. Using an empirically established relationship, which takes into account the magnetic interactions' sensitivity to local distortions and instabilities [37] (i.e., the size variance of the A-site ions or σ^2 [39]), the calculated $T_N(\theta, \sigma^2)$ is compared to the measured value in Fig. 12 as a function of the average size of the A-site cations $\langle r_A \rangle$, which scales linearly with the Ba substitution. The average size progressively increases with Ba doping and can be expressed for the SBMO system as $\langle r_A \rangle = (1-x)r_{\text{Sr}} + (x)r_{\text{Ba}}$ where r_i are the ionic sizes [29]. The difference between the measured and calculated T_N values is less than 1 K for $\text{Sr}_{0.57}\text{Ba}_{0.43}\text{MnO}_3$.

The ferroelectric transition temperature T_C greatly increases from a value that is around room temperature for the $x = 0.43$ sample to 420 K for $\text{Ba} = 0.50$. It has been suggested [40] that this enhancement could be a result of the difference between apical and equatorial Mn–O bond lengths. In SBMO materials, it is interesting to notice that while the Ba substitution has definitely led to larger expansion of the unit cell, the oxygen and Mn atoms shift collectively in such a way that the overly stretched average (Mn–O) bond length for both samples maintain a nearly constant length difference of no more than ~ 0.002 Å at all the examined temperatures between 450–10 K. The marked difference in T_C is attributed to the difference in apical bonds as the in-plane Mn–O₂ bonds in both samples are nearly the same as shown in Fig. 15. Engineering epitaxially strained thin films, which play a role similar to Ba substitution in their bulk counterparts, has been widely used for the purpose of inducing or enhancing ferroelectricity, in general, and for tuning both the T_C and the coupling strength of the order parameters, in particular [17,41–43].

Our previous studies on (Sr, Ca, Ba) MnO_3 manganites [6,37,44] have allowed us to estimate relaxed interatomic distances at room temperature as $[\text{Sr}^{2+} - \text{O}] = 2.691 \pm 0.002$ Å, $[\text{Ba}^{2+} - \text{O}] = 2.783 \pm 0.004$ Å, and $[\text{Mn}^{4+} - \text{O}] = 1.897 \pm 0.002$ Å. By comparing these equilibrium values to the measured bond lengths in the present study we have found that despite being highly strained due to the presence of Ba, the measured $\langle \text{A–O} \rangle$ bond length is $\sim 2.731(2)$ Å for both the compositions $x = 0.43$ and 0.45 in the FE region showing a negligible deviation from the equilibrium value (percent error $\sim 0.03\%$). On the other hand, the MnO_6 octahedra are most sensitive to the Ba substitution and the $\langle \text{Mn–O} \rangle$ bond length for both the $x = 0.43$ and 0.45 samples is significantly stretched beyond its equilibrium value.

IV. CONCLUSIONS

We have investigated the development of spontaneous polarization due to strain-induced displacements in $\text{Sr}_{1-x}\text{Ba}_x\text{MnO}_3$. This effect arises from the opposite displacements of manganese and the surrounding oxygen anions. Quantifying these displacements is critical for understanding the nature of the ferroelectric order. Neutron powder diffraction is of special importance for this work because of its effectiveness

in accurately determining the atomic positions of the light oxygen anions. This is particularly the case when considering the coexistence of magnetism and ferroelectricity.

The ferroelectric order of the $x = 0.43$ and 0.45 compositions is partially suppressed at the onset of magnetic ordering. Below T_N , the energetically favorable ferroelectric distortions are likely suppressed by the gain in energy from maintaining a straight bond angle as close to 180° as possible. The ferroelectric suppression is evidenced by the reduction of the tetragonal order as the c/a ratio drops by ~ 40 , 47 , and 55% of its maximum value for the $x = 0.43$, 0.44 , and 0.45 , respectively. This behavior is similar to that observed in Sakai *et al.*'s SBMO single crystal with a Ba content of 45% [7].

One possible way to characterize the appearance of ferroelectric ordering in SBMO system is to establish a strain parameter based on the optimal length of the Mn–O bond length. We have previously studied the phase diagram of the (Sr–Ca–Ba) MnO_3 system from which the individual relaxed bond lengths were determined. As the Ca substitution (y) in $\text{Ca}_{1-y}\text{Sr}_y\text{MnO}_3$ increases to 0.8 , the structure at room temperature becomes cubic. This critical value can be considered to define the equilibrium room temperature $\text{Mn}^{4+} - \text{O}$ bond length $= 1.897 \pm 0.002$ Å in the cubic perovskite manganite system. Additional substitution of larger cations at the Ca/Sr site is certain to induce strains in a cubic symmetry. The cubic structure accommodates the larger-size ions by stretching the Mn–O bonds to beyond their equilibrium limits as observed in previous work with all compositions with $x < 0.43$. However, as shown for $x = 0.43$ and beyond, the structure must relieve the strains by the sudden displacements of the Mn and oxygen atoms.

The electric polarization is sensitive to small changes in the atomic positions [45] and it has been proposed [7,46] that ferroelectricity in SBMO materials exhibits a spontaneous electric polarization, which can be calculated from the ionic displacements with maximum values comparable to the prototypical BaTiO_3 ($27 \mu\text{C}/\text{cm}^2$ [36]). For instance, for Sakai *et al.*'s single crystal with $x = 0.50$, a value of $P_s \sim 14 \mu\text{C}/\text{cm}^2$ just below T_N is predicted from the thermal evolution of the tetragonal distortion $[(1 - c/a) \sim P_s^2]$ to reach a maximum of $25 \mu\text{C}/\text{cm}^2$ in the FE region [7]. Indeed, from the measured bond lengths and bond angles we have calculated maximum P_s values of 18.4 and $29.5 \mu\text{C}/\text{cm}^2$ with a sharp drop below T_N to 13.6 and $13.4 \mu\text{C}/\text{cm}^2$ for $\text{Sr}_{0.57}\text{Ba}_{0.43}\text{MnO}_3$ and $\text{Sr}_{0.55}\text{Ba}_{0.45}\text{MnO}_3$, respectively.

The larger spontaneous polarization in $\text{Sr}_{0.55}\text{Ba}_{0.45}\text{MnO}_3$ as compared to $\text{Sr}_{0.57}\text{Ba}_{0.43}\text{MnO}_3$ is a result of consistently larger structural distortions as quantified by the (c/a) ratio for the former across different T regions as shown in Fig. 13. It is well known that ferroelectric materials with higher Curie temperature possess larger values of polarization [3], which is also the case in our materials in agreement with previous first-principles [19] and *ab initio* calculations [47] predicting large P_s values in $\text{Sr}_{1-x}\text{Ba}_x\text{MnO}_3$ of $12.8 \mu\text{C}/\text{cm}^2$ and $17 \mu\text{C}/\text{cm}^2$ for BaMnO_3 ($x = 1$) and paramagnetic $\text{Sr}_{0.50}\text{Ba}_{0.50}\text{MnO}_3$, respectively. On the other hand, improper ferroelectrics are known to exhibit small polarization values [11] as in the hexagonal YMnO_3 in which ferroelectricity is geometrically induced with a P_s of $\sim 6 \mu\text{C}/\text{cm}^2$ [14].

Tensile strains were found to favor polar distortions in Ba-doped SrMnO₃ by reducing the energy gap and the simultaneous promotion of strong covalent Mn–O bonding [17,19]. Equivalent strain effects due to increased Ba doping from Sr_{0.57}Ba_{0.43}MnO₃ to Sr_{0.55}Ba_{0.45}MnO₃ not only lead to expanding the stability range of the ferroelectric phase with a higher transition temperature, T_C , but also to decreasing on-site Coulomb repulsion U [48,49] in agreement with the reduced refined magnetic moments of the Mn⁴⁺ ions from their expected $3 \mu_B$ value (t_{2g}^3 , $S = 3/2$) [47]. The calculated moments of the parent compound SrMnO₃ are $2.47 \mu_B$ from a DFT study [49] and $2.7 \mu_B$ from first-principles calculations [18] both of which are in agreement with the experimentally determined value of $2.6 \pm 0.2 \mu_B$ [50]. Similar moment values were reported for SBMO system with 10% Ba substitution where the experimentally refined moment yielded $2.4 \mu_B$ at the lowest measured temperatures [6] whereas moments of $2.6 \mu_B$ [46] and $2.75 - 2.53 \mu_B$ [47] have been estimated for Ba = 50% composition by *ab initio* calculations.

Negative chemical pressure (i.e., tension), which expands the unit cell volume by doping, has varying degrees of influence

on the crystal structures of the manganite materials [48]. This effect could range from the complete suppression of the antiferrodistortive transitions (rotations of oxygen in MnO₆ octahedra) as found in Ba-doped La_{0.5}Sr_{0.5-x}Ba_xMnO₃ [40], for example, to the extreme case observed in this study where it favors the competing ferrodistortive ordering and the displacement of the Mn⁴⁺ ions away from their octahedral centers.

ACKNOWLEDGMENTS

Part of this research conducted at ORNL's Spallation Neutron Source was sponsored by the Scientific User Facilities Division, Office of Basic Energy Sciences, U. S. Department of Energy. Use of the Advanced Photon Source at Argonne National Laboratory was supported by the U. S. Department of Energy, Office of Science, Office of Basic Energy Sciences, under Contract No. DE-AC02-06CH11357. Work at the Materials Science Division at Argonne National Laboratory was supported by the U.S. DOE, Office of Science, Materials Sciences and Engineering Division.

-
- [1] T. Kimura, T. Goto, H. Shintani, and K. Ishizaka, *Nature (London)* **426**, 55 (2003).
- [2] R. Ramesh and N. A. Spaldin, *Nature Mater.* **6**, 21 (2007).
- [3] J. Wang *et al.*, *Science* **299**, 1719 (2003).
- [4] K. F. Wang, J. M. Liu, and Z. F. Ren, *Adv. Phys.* **58**, 321 (2009).
- [5] T. Kimura, S. Kawamoto, I. Yamada, M. Azuma, M. Takano, and Y. Tokura, *Phys. Rev. B* **67**, 180401 (2003).
- [6] O. Chmaissem, B. Dabrowski, S. Kolesnik, J. Mais, D. E. Brown, R. Kruk, P. Prior, B. Pyles, and J. D. Jorgensen, *Phys. Rev. B* **64**, 134412 (2001).
- [7] H. Sakai, J. Fujioka, T. Fukuda, D. Okuyama, D. Hashizume, F. Kagawa, H. Nakao, Y. Murakami, T. Arima, A. Q. R. Baron, Y. Taguchi, and Y. Tokura, *Phys. Rev. Lett.* **107**, 137601 (2011).
- [8] T. Kimura, G. Lawes, T. Goto, Y. Tokura, and A. P. Ramirez, *Phys. Rev. B* **71**, 224425 (2005).
- [9] S. Dong, R. Yu, S. Yunoki, J. M. Liu, and E. Dagotto, *Phys. Rev. B* **78**, 155121 (2008).
- [10] J. Van Den Brink and D. I. Khomskii, *J. Phys.: Condens. Matter* **20**, 434217 (2008).
- [11] G. Giovannetti, S. Kumar, J. van den Brink, and S. Picozzi, *Phys. Rev. Lett.* **103**, 037601 (2009).
- [12] M. H. Qin, Y. M. Tao, M. Zeng, X. S. Gao, S. J. Wu, S. Dong, and J. M. Liu, *Appl. Phys. Lett.* **100**, 052410 (2012).
- [13] M. Mochizuki and N. Furukawa, *Phys. Rev. B* **80**, 134416 (2009).
- [14] C. J. Fennie and K. M. Rabe, *Phys. Rev. B* **72**, 100103 (2005).
- [15] R. E. Cohen, *Nature (London)* **358**, 136 (1992).
- [16] S.-W. Cheong and M. Mostovoy, *Nature Mater.* **6**, 13 (2007).
- [17] S. Bhattacharjee, E. Bousquet, and P. Ghosez, *Phys. Rev. Lett.* **102**, 117602 (2009).
- [18] J. H. Lee and K. M. Rabe, *Phys. Rev. Lett.* **104**, 207204 (2010).
- [19] J. M. Rondinelli, A. S. Eidelson, and N. A. Spaldin, *Phys. Rev. B* **79**, 205119 (2009).
- [20] H. Chen and A. J. Millis, *Phys. Rev. B* **94**, 165106 (2016).
- [21] V. Goian *et al.*, *J. Phys.: Condens. Matter* **28**, 175901 (2016).
- [22] V. Goian, E. Langenberg, N. Marcano, V. Bovtun, L. Maurel, M. Kempa, T. Prokscha, J. Kroupa, P. A. Algarabel, J. A. Pardo, and S. Kamba, *Phys. Rev. B* **95**, 075126 (2017).
- [23] H. Sakai, J. Fujioka, T. Fukuda, M. S. Bahramy, D. Okuyama, R. Arita, T. Arima, A. Q. R. Baron, Y. Taguchi, and Y. Tokura, *Phys. Rev. B* **86**, 104407 (2012).
- [24] T. Negas and R. S. Roth, *J. Solid State Chem.* **1**, 409 (1970).
- [25] A. Huq, J. P. Hodges, O. Gourdon, and L. Heroux, *Z. Kristallogr. Proc.* **1**, 127 (2011).
- [26] A. C. Larson and R. B. Von Dreele, General Structure Analysis System (GSAS), Los Alamos National Laboratory Report LAUR 86-748 (2000).
- [27] B. H. Toby, *J. Appl. Crystallogr.* **34**, 210 (2001).
- [28] J. Goodenough, *Rep. Prog. Phys.* **67**, 1915 (2004).
- [29] R. D. Shannon, *Acta Crystallogr. A* **32**, 751 (1976).
- [30] W. P. Mason and B. T. Matthias, *Phys. Rev.* **74**, 1622 (1948).
- [31] B. Matthias and A. Von Hippel, *Phys. Rev.* **73**, 1378 (1948).
- [32] J. S. Zhou and J. B. Goodenough, *Phys. Rev. Lett.* **94**, 065501 (2005).
- [33] R. Buttner and E. Maslen, *Acta Crystallogr. B* **48**, 764 (1992).
- [34] D. K. Pratt, J. W. Lynn, J. Mais, O. Chmaissem, D. E. Brown, S. Kolesnik, and B. Dabrowski, *Phys. Rev. B* **90**, 140401 (2014).
- [35] Y. Tokura and N. Nagaosa, *Science* **288**, 462 (2000).
- [36] W. Zhong, D. Vanderbilt, and K. M. Rabe, *Phys. Rev. Lett.* **73**, 1861 (1994).
- [37] B. Dabrowski, S. Kolesnik, O. Chmaissem, L. Suescun, and J. Mais, *Acta Phys. Pol., A* **111**, 15 (2007).
- [38] J.-S. Zhou and J. B. Goodenough, *Phys. Rev. B* **77**, 132104 (2008).
- [39] L. M. Rodriguez-Martinez and J. P. Attfield, *Phys. Rev. B* **54**, R15622(R) (1996).
- [40] O. Chmaissem, B. Dabrowski, S. Kolesnik, J. Mais, L. Suescun, and J. D. Jorgensen, *Phys. Rev. B* **74**, 144415 (2006).
- [41] K. J. Choi *et al.*, *Science* **306**, 1005 (2004).

- [42] J. Haeni, P. Irvin, W. Chang, and R. Uecker, *Nature (London)* **430**, 758 (2004).
- [43] E. Langenberg, L. Maurel, N. Marcano, R. Guzmán, P. Štrichovanec, T. Prokscha, C. Magén, P. A. Algarabel, and J. A. Pardo, *Adv. Mater. Interfaces* **4**, 1601040 (2017).
- [44] B. Dabrowski, O. Chmaissem, J. Mais, S. Kolesnik, J. D. Jorgensen, and S. Short, *J. Solid State Chem.* **170**, 154 (2003).
- [45] A. Filippetti and N. A. Hill, *Phys. Rev. B* **65**, 195120 (2002).
- [46] G. Giovannetti, S. Kumar, C. Ortix, M. Capone, and J. van den Brink, *Phys. Rev. Lett.* **109**, 107601 (2012).
- [47] R. Nourafkan, G. Kotliar, and A. M. S. Tremblay, *Phys. Rev. B* **90**, 220405 (2014).
- [48] A. Marthinsen, C. Faber, U. Aschauer, N. A. Spaldin, and S. M. Selbach, *MRS Commun.* **6**, 182 (2016).
- [49] R. Søndenå, P. Ravindran, S. Stølen, T. Grande, and M. Hanfland, *Phys. Rev. B* **74**, 144102 (2006).
- [50] T. Takeda and S. Ohara, *J. Phys. Soc. Jpn.* **37**, 275 (1974).